# CMS Physics Analysis Summary

Contact: cms-pag-conveners-exotica@cern.ch 2020/09/28

# Search for long-lived particles decaying to jets with displaced vertices

The CMS Collaboration

## Abstract

We report the results of a search for long-lived particles produced in pairs in proton-proton collisions at the LHC operating at a center-of-mass energy of $\sqrt{s} = 13$ TeV. The data were collected by the CMS detector during the full Run 2 data taking period from 2015 through 2018, corresponding to a total integrated luminosity of 140 fb$^{-1}$. This search targets long-lived particles with a mean proper decay length between 0.1 and 100 mm that each decay into at least two quarks. The signature is a pair of displaced vertices each formed from many tracks. This search extends a previous CMS search using the 2015 and 2016 dataset, with improvements in background rejection, background estimation techniques, as well as uncertainty estimation. By requiring two reconstructed vertices inside the beam pipe, this search has particularly high sensitivity to decay lengths below 20 mm, which complements similar long-lived search strategies that are less sensitive to such short decay lengths. Results are compared with $R$-parity violating supersymmetry models that predict pair-produced long-lived particles, each decaying into multijet or dijet final states. No events are observed with two reconstructed high-track-multiplicity vertices. For models of long-lived pair-produced neutralinos, gluinos, and top squarks, pair-production cross sections larger than 0.08 fb are excluded at 95% confidence level for masses between 800 and 3000 GeV and mean proper decay lengths between 1 and 25 mm.

# 1 Introduction

Particles with macroscopically-long lifetimes are common in models of physics beyond the standard model (BSM). A diverse array of BSM physics models predict the production of long-lived particles at the CERN LHC including, but not limited to: $R$-parity violating (RPV) supersymmetry (SUSY) [1–4], split SUSY [5–11], hidden valley models [12–14], stealth SUSY [15, 16], as well as models giving rise to dark matter candidates [17–24]. Searches for long-lived particles therefore probe a broad BSM parameter space.

The expansive parameter space calls for an inclusive and model-independent search. This analysis searches for long-lived particles that are produced in pairs and decay into final states with multiple jets containing many charged particles. More concretely, the analysis looks for a unique experimental signature of two vertices, formed from the intersection of multiple charged-particle trajectories, displaced from the interaction region but within the radius of the LHC beam pipe.

As benchmarks, this analysis explores two signal models with distinct final states. The first model represents a minimal flavor violating model of RPV SUSY [2] in which the lightest SUSY particle (LSP) is a long-lived neutralino or gluino that is produced in pairs. This long-lived particle then decays into top, bottom, and strange antiquarks as shown in Fig. 1, resulting in a "multijet" final state signal topology. The second benchmark model is another RPV model in which the pair-produced top squark is the long-lived LSP [3]. Each squark decays into a pair of down-type quarks, resulting in a "dijet" final state signature as also shown in Fig. 1.

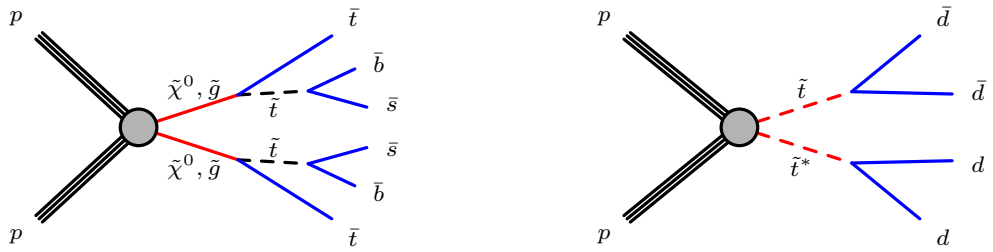


Figure 1: Diagrams of the multijet signal model (left) showing a long-lived neutralino ($\widetilde{\chi}^0$) or gluino ($\widetilde{g}$) decaying into top, bottom, and strange antiquarks via a virtual top squark ($\widetilde{t}$), and the dijet signal model (right) showing a long-lived top squark decaying into two down-type quarks. In both cases, the long-lived particle is the LSP in their respective models.

The displaced vertices are reconstructed from charged particle tracks using a custom vertex reconstruction algorithm. To discriminate the signal from the SM background, we use the separation between the vertex pairs in the plane transverse to the beam direction. This variable distinguishes the signal events, which tend to have well-separated vertex pairs, from background events whose vertices originate from track misreconstruction and have marginal displacements from the beam axis.

We target signals with lifetimes corresponding to a mean proper decay length, $c\tau$, range of 0.1 to 100 mm. Longer lifetimes are generally less accessible since we require the vertices to be reconstructed within the beam pipe radius (20 mm). This search is primarily sensitive to models in which the mass of each long-lived particle exceeds 600 GeV because of a trigger requiring large total momentum projected into the plane perpendicular to the beam direction.

This analysis is an extension of the previous CMS displaced vertex search based on data collected during 2015 and 2016 [25]. The events used for this analysis were collected with the CMS

detector in 2017 and 2018, corresponding to an integrated luminosity of 101 $\text{fb}^{-1}$. The CMS collaboration upgraded its inner pixel tracking detector during the winter technical stop between the 2016 and 2017 run periods [26], providing improvements that benefit this analysis, which relies on track quality in the vertex reconstruction. While the overall analysis strategy remains largely the same as in the previous analysis, improved techniques further reduce background and improve estimations of systematic uncertainties. For example, a new technique to suppress background vertices arising from accidental track intersections from separate primary vertices has been employed to reduce the overall background by 40%; the uncertainty due to the presence of b quarks in the background template construction has been reduced from 41% to 5%, and new techniques provide a more accurate evaluation of signal efficiencies and their corresponding systematic uncertainties. The results from the 2017 and 2018 data are combined with those of the previous 2015 and 2016 CMS displaced vertex search for a total integrated luminosity of 140 $\text{fb}^{-1}$. This analysis complements similar searches that have been performed by the ATLAS and CMS experiments [27–29] with a higher sensitivity to mean proper decay lengths closer to the interaction region between 100 $\mu$m and 15 mm. By requiring two reconstructed vertices inside the beam pipe, this search uniquely probes this region of parameter space using a set of stringent vertex and event selection criteria that results in a background-free search while retaining high signal efficiency for events containing pairs of long-lived particles.

## 2 The CMS detector and event reconstruction

The central feature of the CMS apparatus is a superconducting solenoid of 6 m internal diameter, providing a magnetic field of 3.8 T. Within the solenoid volume are a silicon pixel and strip tracker, a lead tungstate crystal electromagnetic calorimeter (ECAL), and a brass and scintillator hadron calorimeter (HCAL), each composed of a barrel and two endcap sections. Forward calorimeters extend the pseudorapidity coverage provided by the barrel and endcap detectors. Muons are detected in gas-ionization chambers embedded in the steel flux-return yoke outside the solenoid. A more detailed description of the CMS detector, together with a definition of the coordinate system used and the relevant kinematic variables, can be found in Ref. [30].

The vertex reconstruction at the crux of this analysis relies on the innermost detector surrounding the beam pipe, the silicon tracker. This tracker detects charged particles within the pseudorapidity range $|\eta| < 2.5$. It consists of 1,856 silicon pixel and 15,148 silicon strip detector modules. For nonisolated particles with transverse momentum $p_{\text{T}}$ in the range $1 < p_{\text{T}} < 10\,\text{GeV}$ and $|\eta| < 1.4$, the track resolutions are typically 1.5% in $p_{\text{T}}$ and 20–75 $\mu$m in the transverse impact parameter [31]. With the upgraded silicon pixel tracker used in this dataset, the track impact parameter resolution has improved by 25%.

Events of interest are selected using a two-tiered trigger system [32]. The first level is composed of custom hardware processors and the second level consists of a farm of processors running a version of the full event reconstruction software optimized for fast processing.

A particle-flow algorithm [33] aims to reconstruct and identify each individual particle in an event, with an optimized combination of information from the various elements of the CMS detector. The energy of photons is obtained from the ECAL measurement. The energy of electrons is determined from a combination of the electron momentum at the primary interaction vertex as determined by the tracker, the energy of the corresponding ECAL cluster, and the energy sum of all bremsstrahlung photons spatially compatible with originating from the electron track. The energy of muons is obtained from the curvature of the corresponding track and its $\eta$. The energy of charged hadrons is determined from a combination of their momenta

measured in the tracker and the matching ECAL and HCAL energy deposits, corrected for the response function of the calorimeters to hadronic showers. Finally, the energy of neutral hadrons is obtained from the corresponding corrected ECAL and HCAL energies.

Jets are reconstructed offline from particle-flow candidates clustered using the anti-$k_T$ algorithm [34, 35] with a distance parameter of 0.4. Jet momentum is determined as the vectorial sum of all particle momenta in the jet, and is found from simulation to be, on average, within 5 to 10% of the true momentum over the whole $p_T$ spectrum and detector acceptance. Additional proton-proton interactions within the same or nearby bunch crossings (pileup) can contribute additional tracks and calorimetric energy depositions, increasing the apparent jet momentum. To mitigate this effect, tracks identified to be originating from pileup vertices are discarded and an offset correction is applied to correct for remaining contributions. Jet energy corrections are derived from simulation studies so that the average measured response of jets becomes identical to that of particle level jets. In situ measurements of the momentum balance in dijet, photon+jet, Z+jet, and multijet events are used to determine any residual differences between the jet energy scale in data and in simulation, and appropriate corrections are made [36]. We reject jets with parameters consistent with misidentified leptons, which may include misreconstructed electrons or muon candidates.

## 3 Event samples

Events in both data and simulation are selected using a trigger requiring $H_T > 1050\,\text{GeV}$, where $H_T$ is the scalar sum of the jet $p_T$ for jets with $p_T > 40\,\text{GeV}$ and $|\eta| < 2.5$.

Signal events were simulated using PYTHIA 8.230 [37] with NNPDF3.1LO [38] providing the parton distribution functions (PDF) and the CP2 tune [39] is used to model the underlying event. The samples are produced with a range of masses $m$ ($400 \leq m \leq 3000\,\text{GeV}$) and mean proper decay lengths $c\tau$ ($0.1 \leq c\tau \leq 100\,\text{mm}$). The trigger efficiency is almost 100% for signal models where the mass of the long-lived particle is 1200 GeV or larger. For masses near 600 GeV, the measured trigger efficiency is approximately 50%.

Background events arising from SM processes come entirely from dijet events, multijet events, and events with pair-produced top quarks that contain enough jet activity to satisfy the $H_T$ trigger requirements. These background samples are simulated using MADGRAPH5_aMC@NLO 2.4.2 [40] with the NNPDF3.0 [41] PDF set at leading order with MLM merging [42]. PYTHIA 8.230 [37] was used to simulate the hadronization and showering with the CP5 tune [39] providing the underlying event model.

Both the background and signal samples use a GEANT4-based [43] simulation for the CMS detector response. Minimum bias events are mixed with the hard interaction in simulated events to match the observed pileup distribution in data.

## 4 Event preselection

To ensure that the trigger is well-behaved, an additional offline requirement of $H_T > 1200\,\text{GeV}$ is imposed. This provides a stable 98% trigger efficiency in both data and simulation. We also require at least four reconstructed jets, each with $p_T > 20\,\text{GeV}$ and $|\eta| < 2.5$.

# 5 Vertex reconstruction and selection

The displaced vertices are formed from charged-particle tracks. The first step is the selection of tracks reconstructed from the electrical signals ("hits") due to charged particles traversing the silicon tracker layers. To ensure reconstructed tracks are of high quality, we require tracks to have: $p_{\mathrm{T}}$ of at least 1 GeV; hits measured in the innermost layer of the pixel detector and at least one additional pixel layer; and hits measured in at least six layers of the silicon strip detector. These requirements reduce the mean uncertainty in the transverse impact parameter of the tracks to around 72 $\mu$m, a reduction of approximately 20%. One final requirement is that the magnitude of the impact parameter in the transverse plane with respect to the beam spot divided by its uncertainty, denoted $d_{\mathrm{xy}}/\sigma_{d_{xy}}$, be at least 4. This condition favors tracks with large impact parameters, thereby suppressing the SM background.

The next step in the vertex reconstruction procedure is to generate seed vertices from all pairs of tracks that satisfy the track selection criteria. The Kalman filter method is used to form a vertex from two or more tracks. The vertex is considered valid if its $\chi^2$ per degree of freedom is less than 5. If two vertices share a track and the three-dimensional distance between the vertex pair is less than 4 times the uncertainty in that distance, these are considered compatible and a vertex fit is applied to the complete set of tracks from both vertices. If the resulting fit satisfies the $\chi^2$ requirement, the two vertices are replaced by one single merged vertex. Otherwise, the two vertices remain separated, requiring a track arbitration step to decide which vertex is assigned the shared track. The track arbitration depends on the value of the track's three-dimensional impact parameter significance with respect to each of the vertices. If both impact parameters are within 1.5 standard deviations of both vertices, the shared track is assigned to the vertex with the larger number of tracks already; if the track has an impact parameter that is more than 5 standard deviations from either vertex, the shared track is removed from that vertex; otherwise, the shared track is assigned to the vertex to which it has the smaller impact parameter significance. When a track is dropped from a vertex, that vertex is refit with its remaining tracks and replaced with a new vertex if the fit satisfies the $\chi^2$ requirement, otherwise the vertex is erased entirely. Pairs of vertices are merged iteratively following this algorithm until no two vertices share a track.

Occasionally, a vertex is formed from the accidental intersection of tracks that originate from separate pileup vertices. As a final step in the reconstruction to suppress these, we remove any track if the vertex position along the beam axis shifts appreciably when the track is dropped from the vertex fit. The threshold for removal is a 50 $\mu$m shift. This additional procedure is a new refinement in this analysis with respect to the previous CMS result and removes more than 40% of background vertices in simulation with minimal impact on signal efficiency.

We select vertices with features consistent with a signal vertex by requiring the vertices to have: at least five tracks; an $x$-$y$ position inside the beam pipe, within a radius of 20.9 mm, to suppress background vertices arising from interactions with material; an $x$-$y$ displacement from the beam axis, defined as $d_{\mathrm{BV}}$, of at least 100 $\mu$m to suppress background from displaced primary vertices; and an uncertainty in $d_{\mathrm{BV}}$ of less than 25 $\mu$m to select vertices formed from high quality tracks with large opening angle. This requirement suppresses vertices from b jets, which tend to have narrow opening angles.

This search focuses on signal models with pair-produced long-lived particles, so we require that events have two vertices. Few events in the background contain even one reconstructed displaced vertex; occurrences of higher vertex multiplicity events are even rarer. Simulations of background predict fewer than one event in the two-vertex search region for 101 fb$^{-1}$ of

data. However, a reliable measurement of the signal strength in data requires a more precise estimation of the background, which we evaluate from data.

While signal vertices must have at least five tracks, vertices composed of three or four tracks function as useful control samples to validate the background estimation method. Events with a single 3-track or 4-track vertex are more common than events with a $\geq$5-track vertex by a factor of 30 and 6, respectively; moreover, the large yield dwarfs any potential contamination by signal, so they provide a nearly pure background sample. As an example, for a multijet signal of mass 800 GeV and lifetime 10 mm, the expected signal contamination at the currently excluded cross section of 0.15 fb is less than one event in the 3-track one-vertex sample and two events in the $\geq$5-track one-vertex sample. Distributions of event-level variables (e.g. $H_{\mathrm{T}}$, jet multiplicity) and vertex-level variables (e.g. $d_{\mathrm{BV}}$, uncertainty in $d_{\mathrm{BV}}$) are similar for events with 3, 4, and $\geq$5-track vertices in both simulation and data. Therefore, vertices with lower track multiplicity are expected to provide a reliable approximation for the $\geq$5-track vertex event sample. Table 1 shows the event yields in the control regions.

Table 1: Event yields in the control regions in 101 fb$^{-1}$ of data. The "one-vertex" events correspond to events containing exactly one vertex with the specified number of tracks. The "two-vertex" events have two or more vertices containing the specified numbers of tracks. We seek the signal in the $\geq$5-track two-vertex sample.

| Event category | 3-track | 4-track $\times$ 3-track | 4-track | $\geq$5-track |
|---|---|---|---|---|
| one-vertex | 61818 | — | 14730 | 2211 |
| two-vertex | 185 | 101 | 12 | See Sec. 10 |

# 6 Search strategy

We select events that contain at least two vertices each with 5 or more tracks to search for pair-produced long-lived particles. We use the distance between the vertices in the $x$-$y$ plane, defined as $d_{\mathrm{VV}}$ as shown in Fig. 2, as the discriminating variable between signal and the SM background. In signal events, the pair-produced long-lived particles tend to be emitted back-to-back, resulting in larger vertex separations than in the background where $d_{\mathrm{VV}}$ tends to be small. In events with more than two vertices, the two vertices with the highest number of tracks are chosen for the $d_{\mathrm{VV}}$ calculation. If there is a tie in the number of tracks, a mass value is assigned to the vertex, reconstructed from the momenta of the tracks associated with the vertex, and the one with the higher mass is chosen. However, in the 2017 and 2018 data, we observe no events with more than two vertices.

The $d_{\mathrm{VV}}$ distribution of the background cannot be reliably ascertained from simulations. The sample sizes are inadequate and background vertices are sensitive to the misreconstruction of tracks, which is difficult to accurately replicate in simulation. Thus we construct a $d_{\mathrm{VV}}$ background template using one-vertex events in data, as described in Section 8. Figure 3 compares the $d_{\mathrm{VV}}$ distributions for simulated multijet signals of various mean proper decay lengths, LSP mass of 800 GeV, and production cross section of 0.3 fb overlaid with the background template derived from data. The background peaks near 0.3 mm and has a 3% probability of appearing above 0.7 mm where most signal events are found.

Ultimately, the background and signal templates are fit to the $d_{\mathrm{VV}}$ distribution observed in data in order to extract the signal yield. The fit uses three $d_{\mathrm{VV}}$ bins: 0-0.4 mm, 0.4-0.7 mm, and 0.7-40 mm. This binning scheme maximizes the signal significance in models with lifetimes in the 0.1 to 100 mm range.

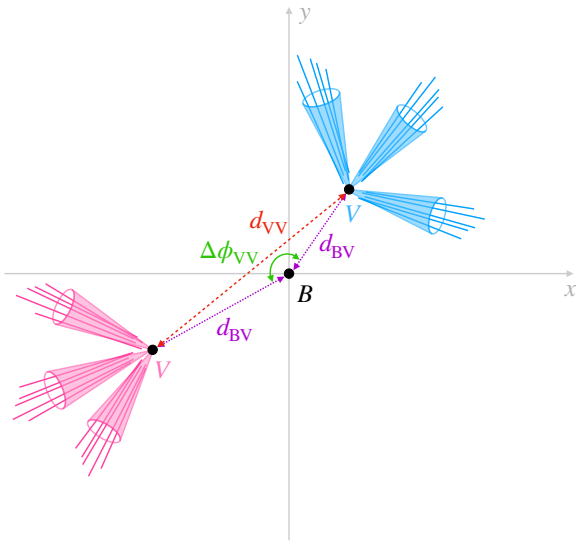


Figure 2: Cartoon diagram of an event with two signal vertices with the beamspot $B$ at the origin. The beam direction is perpendicular to the $x$-$y$ plane shown. The distance between the vertices is defined as $d_{VV}$. The distance from the beamspot to the vertices is defined as $d_{BV}$ and the angle between the vertices with respect to the beamspot is defined as $\Delta\phi_{VV}$.

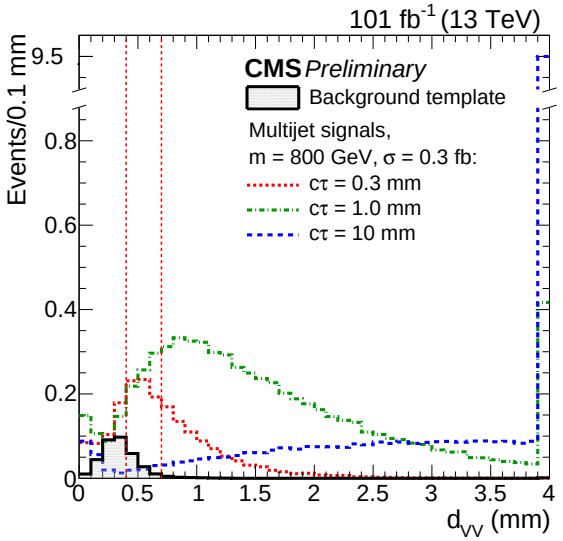


Figure 3: The distribution of distances between vertices in the $x$-$y$ plane, $d_{VV}$, for simulated multijet signals with mass of 800 GeV, production cross section of 0.3 fb, and $c\tau = 0.3$, 1.0, and 10 mm with the background template distribution overlaid. The last bin includes the overflow events. The two vertical red dashed lines delineate the boundaries of the bins used in the fit.

# 7 Signal efficiency measurement

To study the signal vertex reconstruction efficiency, we manually displace tracks from the primary vertex to produce artificial signal-like vertices in data and background simulation samples and then apply the reconstruction procedure. Starting from events satisfying the trigger and offline preselection requirements that also have a well-reconstructed primary vertex, we randomly select reconstructed light parton or b quark jets that have $p_{\mathrm{T}} > 50\,\mathrm{GeV}$ and at least four matched particle-flow candidate tracks. The jets are identified as a light or b quark jet based on their heavy flavor jet tagger discriminator value [44]. The tracks associated with the selected jets are then displaced in the direction defined by the vector sum of the selected jet momenta. The displacement vector direction is smeared to capture the mismeasurement from tracking inefficiency or missing neutral particles. The track impact parameter resolutions in simulation are scaled to match data as a function of $p_{\mathrm{T}}$ and $\eta$. After track selection, vertex reconstruction, and vertex selection, we compute the fraction of events passing the event selection criteria that also contain a vertex reconstructed near the expected location. This efficiency accounts for the track reconstruction and selection efficiencies in addition to the one from vertex reconstruction.

For the dijet signals, we replicate the signal by displacing the tracks associated with two light jets by a magnitude sampled from an exponential distribution with a configurable scale parameter $c\tau$ restricted to values between 0.3 and 20 mm, which is characteristic of vertices that would enter the most signal-sensitive region in $d_{\mathrm{VV}}$ (0.7 mm-40 mm). The efficiency is suppressed when the two jet momentum vectors are in opposite directions and parallel to the displacement because of the large resulting uncertainty in vertex position. We therefore reweight the efficiency of these events relative to the others based on their relative proportions in the signal simulation. The differences in vertex reconstruction efficiency between data and simulation arise mainly from modeling of the number of tracks satisfying the impact parameter requirement. The vertex reconstruction efficiency differences range from 5% for the longest lifetimes to 16% for the shortest.

For multijet signals, we replicate the signal by displacing the tracks associated with three light jets and two b-quark jets. The displacement is sampled from the signal simulation displacement distribution for events with $d_{\mathrm{VV}}$ between 0.7 mm-40 mm. Here, the reconstruction efficiency reaches 50% in both data and simulation when six or seven selected tracks emanate from the vertex and is over 90% efficient for a vertex with at least 12 selected tracks. It is almost always the case for vertices with large displacements to have many tracks, and consequently the difference between data and simulation efficiency for these vertices is small. Vertices near the beam axis, however, have fewer selected tracks due to the track impact parameter significance requirement, leading to lower overall vertex reconstruction efficiencies of 40% to 60% for samples with lifetimes of 100 $\mu$m. On average, data has two fewer selected tracks than simulation, resulting in lower vertex reconstruction efficiency in data for the short lifetime samples. In the multijet case, we measure a vertex reconstruction efficiency difference between the data and simulation to be within 0.1% and 14%, with better agreement at longer lifetimes.

The differences in the vertex reconstruction efficiencies between data and simulation in both multijet and dijet signals are used to correct the signal simulation yields. The correction is applied twice to account for each displaced vertex in the signal. Figure 4 shows the signal efficiency in both multijet and dijet signals after applying all event and vertex requirements for events containing a pair of vertices with further corrections provided by the procedure described. The increase in efficiency with mass comes from the higher probability of satisfying the trigger and offline $H_{\mathrm{T}}$ requirements. Initially, the efficiency increases with lifetime while mov-

ing away from the prompt region, but decreases for large lifetimes because of the requirement that vertices lie within the beam pipe.

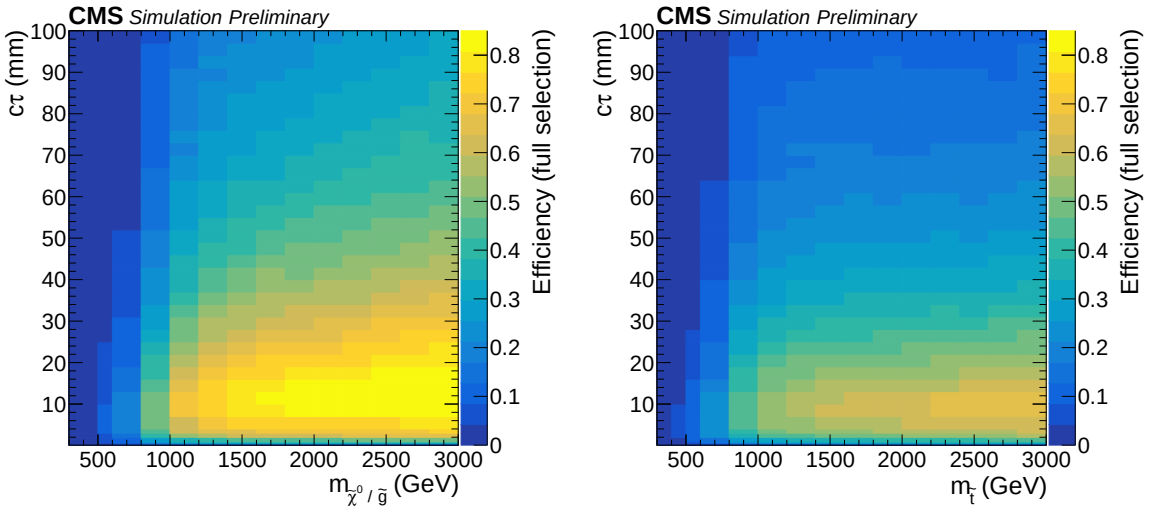


Figure 4: Multijet (left) and dijet (right) signal efficiencies as a function of the signal mass and lifetime for events satisfying all event and vertex requirements with corrections based on systematic differences in the vertex reconstruction efficiency between data and simulation.

## 8 Background template

In the background, most vertices include at least one misreconstructed track that endows the vertex with a displacement away from the interaction point. Individual well-reconstructed b jets do not contribute a significant number of background vertices on their own due to the requirement on the vertex $d_{\mathrm{BV}}$ uncertainty. Instead, background events contain two misreconstructed vertices whose displacements are independent of one another except for correlations due to events with b quarks. This correlation is handled with separate treatments of events with b tagged jets and events without b tagged jets. The independence of the two vertex displacements is a crucial feature as it offers a method with which to predict the shape of the search variable distribution, $d_{\mathrm{VV}}$, in two-vertex events using information from events containing only one vertex. The constructed template, denoted as $d_{\mathrm{VV}}^{\mathrm{C}}$, provides the predicted two-vertex yields in each of the three $d_{\mathrm{VV}}$ search bins. Events with one vertex are more common than two-vertex events by a factor of 100 to 1000 as shown in Table 1. This abundance of one-vertex events enables a template with high statistical precision.

Constructing a single value of $d_{\mathrm{VV}}^{\mathrm{C}}$ requires the following elements: two values of $d_{\mathrm{BV}}$, one for each vertex, and one $\Delta\phi_{\mathrm{VV}}$ value to specify the azimuthal angle between the two vertices, both of which are illustrated in Fig. 2. Repeated sampling of $d_{\mathrm{BV}}$ and $\Delta\phi_{\mathrm{VV}}$ forms the preliminary shape template $d_{\mathrm{VV}}^{\mathrm{C}}$, subject to an additional correction for merging overlapping vertices. The sampling repeats until the total number of entries in the final $d_{\mathrm{VV}}^{\mathrm{C}}$ template is equal to 20 times the number of one-vertex events in data. The oversampling reduces the statistical uncertainty and increases the probability of adequately probing the tail of the $d_{\mathrm{BV}}$ distribution. The details of the input variables to the $d_{\mathrm{VV}}^{\mathrm{C}}$ template along with correction will be described in the paragraphs that follow.

The distribution of $d_{\mathrm{BV}}$ in $\geq$5-track one-vertex events is shown in Fig. 5, which also overlays the $\geq$5-track one-vertex $d_{\mathrm{BV}}$ distributions for simulated signal samples of varying lifetimes.

The effects of signal contamination are negligible from existing upper limits on the signal cross sections of 0.3 fb due to the much larger one-vertex background at low $d_{\mathrm{BV}}$.

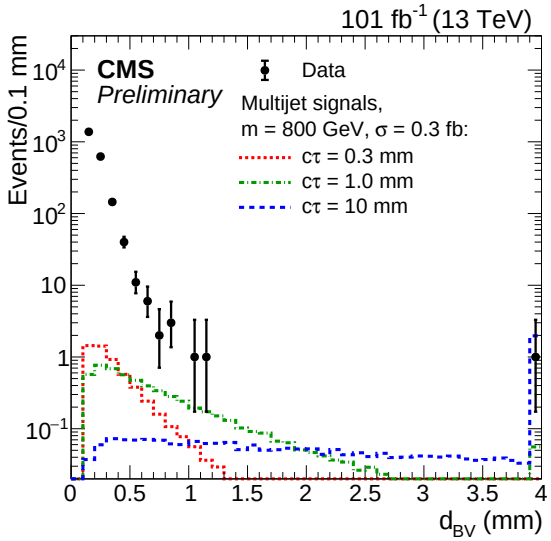


Figure 5: The distribution of $d_{\mathrm{BV}}$ for $\geq$5-track one-vertex events in data and simulated multijet signal samples with mass of 800 GeV, production cross section of 0.3 fb, and $c\tau = 0.3$, 1.0, and 10 mm. The last bin includes the overflow events.

We observe a slight tendency for vertex displacement vectors to be perpendicular to jet momentum vectors. The distribution of azimuthal angles between all possible pairs of jets in an event, denoted as $\Delta\phi_{\mathrm{JJ}}$, is roughly uniform with a preference for high-angle separations, which roughly corresponds to the distribution of $\Delta\phi_{\mathrm{VV}}$ for events with two low-track-multiplicity vertices. Since the $\Delta\phi_{\mathrm{JJ}}$ distribution is consistent across events containing vertices with different track multiplicities, the $\Delta\phi_{\mathrm{JJ}}$ distribution from the high statistics 3-track one-vertex events is used to sample a $\Delta\phi_{\mathrm{VV}}$ angle for the $d^{\mathrm{C}}_{\mathrm{VV}}$ template construction.

The template construction procedure occasionally results in small separations between the vertices. However, small $d^{\mathrm{C}}_{\mathrm{VV}}$ values are normally suppressed by the vertex reconstruction algorithm, which merges nearby vertices. To capture this behavior, we correct the $d^{\mathrm{C}}_{\mathrm{VV}}$ template using the survival efficiency of vertex pairs as a function of their separation. This efficiency is estimated in data from the fraction of initial 3-track vertex pairs that remain after merging.

Single b jet vertices rarely satisfy the requirement on the $d_{\mathrm{BV}}$ uncertainty because the narrow collimation of tracks from the b jet results in poor $d_{\mathrm{BV}}$ resolution. However, events with b quarks are four times more likely to have a displaced vertex than those without because the b jet tracks more often satisfy the $d_{\mathrm{xy}}/\sigma_{d_{xy}}$ requirement. Moreover, in simulation, b quark events are observed to have larger $d_{\mathrm{BV}}$ on average by $39\pm2$ $\mu$m in 3-track vertex events, $37\pm6$ $\mu$m for 4-track vertex events, and $21\pm17$ $\mu$m in $\geq$5-track vertex events. For reference, the $d_{\mathrm{BV}}$ distribution has a typical mean of 200 $\mu$m. Thus, events with b quark pairs introduce correlations in the $d_{\mathrm{BV}}$ of vertex pairs that are not captured in the template construction. This effect is handled by identifying b quarks using the DeepJet tagging algorithm [44]. Separate $d^{\mathrm{C}}_{\mathrm{VV}}$ templates are constructed in which the events have been sorted into two sets: events that contain at least one tagged b jet and events in which no jet was identified as a b jet by the tagging algorithm. These templates are combined into a single template by weighting them according to the expected fraction of two-vertex events with and without b quarks. The percentage of b quark events is determined by using the b jet identification efficiencies and misidentification probabilities to

relate b tagged events to b quark events. The percentages of b quark events are 85% in 3-track two-vertex events, 89% in 4-track two-vertex events, and 95% in $\geq$5-track two-vertex events. This procedure leads to a 53% enhancement in the yield in the third $d_{\mathrm{VV}}^{\mathrm{C}}$ bin (0.7 mm-40 mm).

We extract the signal yield from a fit for the normalizations of the signal and background templates to the observed $d_{\mathrm{VV}}$ distribution. In the background-only fit, which is also used to fit data in the control regions, the template is normalized to the total two-vertex event yield observed in data. In situations where no two-vertex events are observed, the template is normalized using the squared vertex reconstruction efficiency for events with b quarks and events without b quarks, corrected for the survival efficiency of vertex pairs. We validate the use of the latter normalization in the 3-track two-vertex control sample in which the observed yield agrees with the predicted yield with a ratio of $1.02 \pm 0.07$.

Figure 6 compares the background templates to the observed two-vertex $d_{\mathrm{VV}}$ distributions. The yields in each of the three $d_{\mathrm{VV}}^{\mathrm{C}}$ bins in data are consistent with predictions from the template.

# 9 Systematic uncertainties

## 9.1 Signal-related systematic uncertainties

Since the fit uses signal $d_{\mathrm{VV}}$ templates from simulation, potential differences between data and simulation give rise to systematic uncertainties. The dominant uncertainty comes from the vertex reconstruction efficiency, with other effects such as the PDF uncertainty in the simulation, pileup, jet energy resolution and scale, integrated luminosity, trigger efficiency, and run conditions affecting jet efficiency providing smaller contributions.

We assign a systematic uncertainty equal to the size of the correction of the signal vertex reconstruction efficiency described in Sec. 7, along with additional uncertainties associated with variations to the procedure. The systematic uncertainty assigned for each signal point then falls within the range of 11% to 41% for dijet signals and 1% to 36% for multijet signals. In general, the greater uncertainty in dijet signals comes from their reduced efficiency due to fewer tracks from the decay point.

The remaining systematic uncertainties related to the signal efficiency are much smaller. The impact of the PDF uncertainty on the signal reconstruction efficiency is estimated by generating simulation samples reweighting 100 NNPDF replica sets [45]. The relative uncertainty is obtained from the 68% interval of the signal acceptance of these 100 replica sets to the interval midpoint, yielding a range of uncertainty between 1% and 8%, depending primarily on the signal point mass due to the underlying uncertainty in the parton luminosities that varies with the mass of the particle [38].

The uncertainty in the integrated luminosity is 2.3% in 2017 [46] and 2.5% in 2018 [47]. Uncertainties in the jet energy scale can affect the probability of satisfying the offline $H_{\mathrm{T}}$ and jet $p_{\mathrm{T}}$ requirements. Variations of the jet energy scale result in changes in the signal efficiency of 5% or less for all signal sample masses and lifetimes. Similarly, variations of the jet energy resolution result in differences of 2% or less in the signal efficiency. The uncertainty in the signal efficiency due to pileup is 2%. The trigger efficiency differences between data and simulation contribute an uncertainty of 1%. Certain run conditions during the data collection led to inefficiencies in the electromagnetic and hadronic calorimeters affecting jets in parts of the detector, ultimately contributing 1% uncertainty for each separate issue.

Table 2 summarizes the systematic uncertainties related to the signal models. We assume no

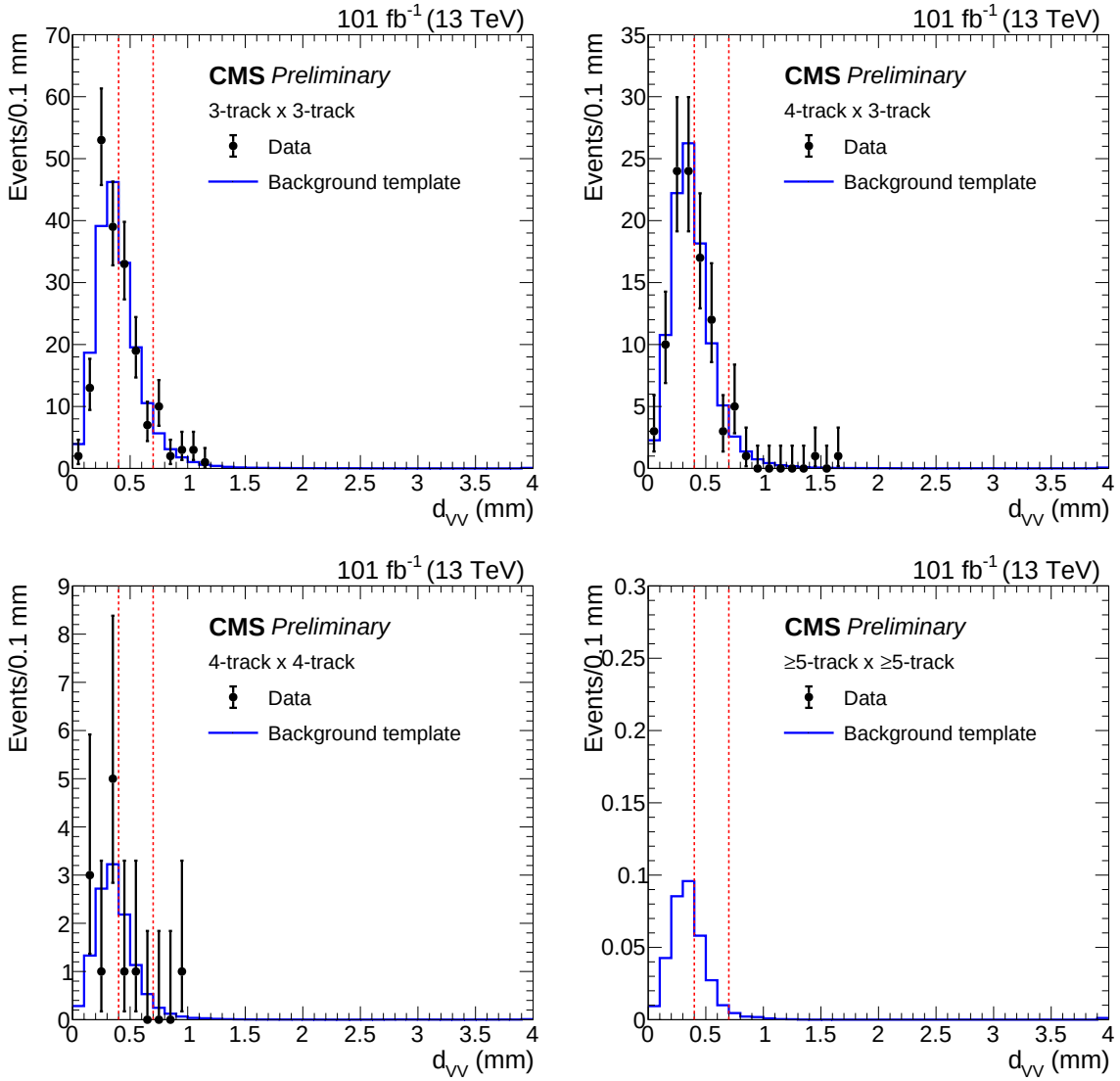


Figure 6: Distribution of the $x$-$y$ distances between vertices, $d_{\mathrm{VV}}$, for 2017 and 2018 data, overlaid on the background template $d_{\mathrm{VV}}^{\mathrm{C}}$ constructed from one-vertex events in data normalized to the two-vertex data for events with 3-track vertices (top left), events with exactly one 4-track vertex and one 3-track vertex (top right), and events with 4-track vertices (bottom left). The background template $d_{\mathrm{VV}}^{\mathrm{C}}$ for $\geq$5-track two-vertex events (bottom right) is normalized using one-vertex event information as described in the text. The two vertical red dashed lines delineate the three $d_{\mathrm{VV}}$ bins.

correlations between the different contributions and obtain an overall systematic uncertainty by adding each value in quadrature.

Table 2: Signal-related systematic uncertainties for dijet and multijet signal models. The overall uncertainty is the sum in quadrature of the individual uncertainties.

| Systematic effect | Dijet uncertainty (%) | Multijet uncertainty (%) |
|---|---|---|
| Vertex reconstruction | 11–41 | 1–36 |
| PDF uncertainty | 1–8 | 1–8 |
| Integrated luminosity | 2–3 | 2–3 |
| Jet energy scale | 5 | 5 |
| Jet energy resolution | 2 | 2 |
| Pileup | 2 | 2 |
| Trigger efficiency | 1 | 1 |
| Changes in run conditions | 1 | 1 |
| Overall | 13-42 | 7-36 |

## 9.2 Systematic uncertainties in background template

Systematic uncertainties in the background template come from effects that modify the shape of the constructed $d_{VV}^{C}$ distribution away from the shape of the true two-vertex $d_{VV}$ distribution. The 3-track vertex control sample provides a way to assess these differences with sufficient statistical precision. Thus, within each of the three bins in the $d_{VV}^{C}$ template in the 3-track vertex control sample, we evaluate the ratio of the yield predicted by the template to the true observed two-vertex yield in data, referred to as the closure, and take the deviation from unity as a measure of the systematic uncertainty for each $d_{VV}^{C}$ bin. We find the $d_{VV}/d_{VV}^{C}$ ratio is $0.99 \pm 0.10$ in the 0-0.4 mm bin, $0.93 \pm 0.12$ in the 0.4-0.7 mm bin, and $1.38 \pm 0.32$ in the 0.7-40 mm bin.

The normalization of the background template was calculated following the same principle as the template itself. Thus, the same variations are taken to assess the sensitivity of the normalization factor to determine a systematic uncertainty. The dominant contributor driving the size of this uncertainty is the vertex pair survival efficiency correction, modified to provide an absolute efficiency. This systematic uncertainty is assigned equally to all three bins.

We must test the assumption that the closure in 3-track events implies closure in $\geq$5-track events with variations in the different inputs and corrections to the template. The template shape is particularly sensitive to the vertex pair survival efficiency correction, which uses the $d_{VV}$-dependent efficiency for vertex pairs to survive. To vary this procedure and derive an alternative efficiency curve, we consider seed vertices formed from all possible combinatorial track quintuplets, i.e. five tracks. We construct the $d_{VV}^{C}$ template with the resulting efficiency curve using this variation and assign the relative difference per bin of the template as the systematic uncertainty.

When constructing the background template, the angular separation between vertices $\Delta\phi_{VV}$ is modeled from the $\Delta\phi_{JJ}$ distribution in 3-track vertices. The $\Delta\phi_{JJ}$ distributions in $\geq$5-track one-vertex events and 3-track one-vertex events are consistent, but this does not exclude differences in the angles between jets and vertices. To gauge this effect, we construct the template by sampling the $\Delta\phi_{VV}$ value from a uniform distribution. The relative difference of the resulting template from the nominal template in each $d_{VV}^{C}$ bin is taken as the systematic uncertainty.

The b tag efficiencies and fake rates are determined using simulated events in the phase space relevant to this analysis, and efficiency correction factors are applied to match the efficiencies

and fake rates in data. We vary these based on measurements of the $p_T$-dependent b tagging efficiency [44] and take the relative difference of the resulting template as the systematic uncertainty. Similarly, we vary the b quark fraction in $\geq$5-track vertex events within the ranges observed in 3-track and 4-track vertex events, assigning the systematic uncertainty as the relative difference in the resulting template.

Table 3 summarizes the systematic uncertainty for each of these components for each $d_{VV}$ bin. We assume no correlations between these different effects and add all values and their uncertainties in quadrature to obtain the overall systematic uncertainty in each bin. The limits are computed assuming that the background systematic uncertainty in the first bin is anti-correlated with the second and third bins to preserve the normalization of the template. Additionally, each bin is fully correlated across the different data taking periods while the statistical components of each bin are assumed to be uncorrelated.

Table 3: Systematic shifts and the statistical uncertainties on them in the background prediction in each $d_{VV}^{C}$ bin arising from varying the construction of the $d_{VV}^{C}$ template. The overall systematic uncertainty and its statistical uncertainty in each bin is the sum in quadrature of the shifts assuming no correlations among the sources.

| | Shift $\pm$ Statistical Uncertainty (%) | | |
|---|---|---|---|
| Systematic effect | 0–0.4 mm | 0.4–0.7 mm | 0.7–40 mm |
| Closure in 3-track control sample | $1 \pm 10$ | $7 \pm 12$ | $38 \pm 32$ |
| $\geq$5-track template normalization factor | $23 \pm 7$ | $23 \pm 7$ | $23 \pm 7$ |
| Difference from 3-track vertices to $\geq$5-track vertices: | | | |
| Modeling of vertex pair survival efficiency | $9 \pm < 0.5$ | $20 \pm 1$ | $25 \pm 5$ |
| Modeling of $\Delta\phi_{VV}$ | $3 \pm < 0.5$ | $6 \pm 1$ | $5 \pm 3$ |
| Variation of b-tag fraction | $1 \pm < 0.5$ | $3 \pm 1$ | $5 \pm 3$ |
| Variation of b-tag correction factors | $0 \pm < 0.5$ | $0 \pm < 0.5$ | $1 \pm 1$ |
| Overall | $25 \pm 12$ | $32 \pm 14$ | $51 \pm 33$ |

# 10 Results and statistical interpretation

Table 4 summarizes the predicted $\geq$5-track two-vertex event yields in each of the three $d_{VV}$ bins from the background and signal templates for three multijet signal lifetime points as well as the observation in data. No $\geq$5-track two-vertex events were observed in the 2017 and 2018 data.

Table 4: Predicted yields for the background-only normalized template, the predicted yields for multijet signals with mass of 800 GeV, production cross section of 0.3 fb, and $c\tau = 0.3, 1.0,$ and 10 mm, and the observed yield in each $d_{VV}$ bin. The uncertainty in the signal yields and the systematic uncertainty in the background prediction reflect the systematic uncertainties given in Tables 2 and 3, respectively.

| | | Predicted multijet signal yields | | | |
|---|---|---|---|---|---|
| $d_{VV}$ range | Predicted background yield | 0.3 mm | 1.0 mm | 10 mm | Observed |
| 0–0.4 mm | $0.235 \pm 0.003$ (stat) $\pm 0.059$ (syst) | $0.7 \pm 0.2$ | $0.7 \pm 0.1$ | $0.20 \pm 0.02$ | 0 |
| 0.4–0.7 mm | $0.096 \pm 0.003$ (stat) $\pm 0.031$ (syst) | $0.8 \pm 0.2$ | $1.1 \pm 0.2$ | $0.10 \pm 0.01$ | 0 |
| 0.7–40 mm | $0.011 \pm 0.001$ (stat) $\pm 0.006$ (syst) | $0.8 \pm 0.2$ | $5.4 \pm 0.9$ | $12 \pm 1$ | 0 |

To extract the signal yield from the data, we perform a binned shape fit using an extended maximum likelihood with three $d_{VV}$ bins. Signal $d_{VV}$ templates come directly from simulation with a template for each signal model, mass, and lifetime point. The background $d_{VV}^{C}$ template is constructed from the one-vertex events in data. The overall normalizations of the signal and

background templates are free parameters of the fit under the constraint that the signal yield is nonnegative. The results obtained from the fit depend on the relative yields in the three $d_{VV}$ bins and their systematic uncertainties. The 2017 and 2018 datasets are treated independently and combined in the fit.

The upper limits on the signal cross section are determined by first assuming a uniform Bayesian prior for the cross section. For each signal mass and lifetime point, the signal efficiency is constrained by a log-normal prior with a corresponding width as determined from the overall systematic uncertainty in the signal processes as summarized in Table 2. The shape uncertainty in the signal template arises from the statistical uncertainty of the simulation. For the background template, a log-normal prior is taken for each $d_{VV}^{C}$ bin for each dataset year with widths specified in Table 3.

The final fit combines this dataset together with limits set in 2015 and 2016 to achieve the full Run 2 result. The correlation between these datasets are treated the same as the correlation between the 2017 and 2018 datasets. Figure 7 shows the full Run 2 95% confidence level (CL) upper limits on the product of the pair-production cross section with the square of the branching fraction ($\sigma\mathcal{B}^2$), as a function of mass and mean proper decay length. The exclusion curves overlaid assume the gluino and top squark pair production cross sections at $\text{NNLO}_{\text{approx}}$+NNLL precision [48–50]. For the neutralino, the production cross sections are computed at NLO+NLL precision in a limit of mass-degenerate higgsino states $\tilde{\chi}_1^{\pm}$, $\tilde{\chi}_1^0$, and $\tilde{\chi}_2^0$ with all the other sparticles assumed to be heavy and decoupled [51, 52]. For all models, we assume a 100% branching fraction to the specified decay mode.

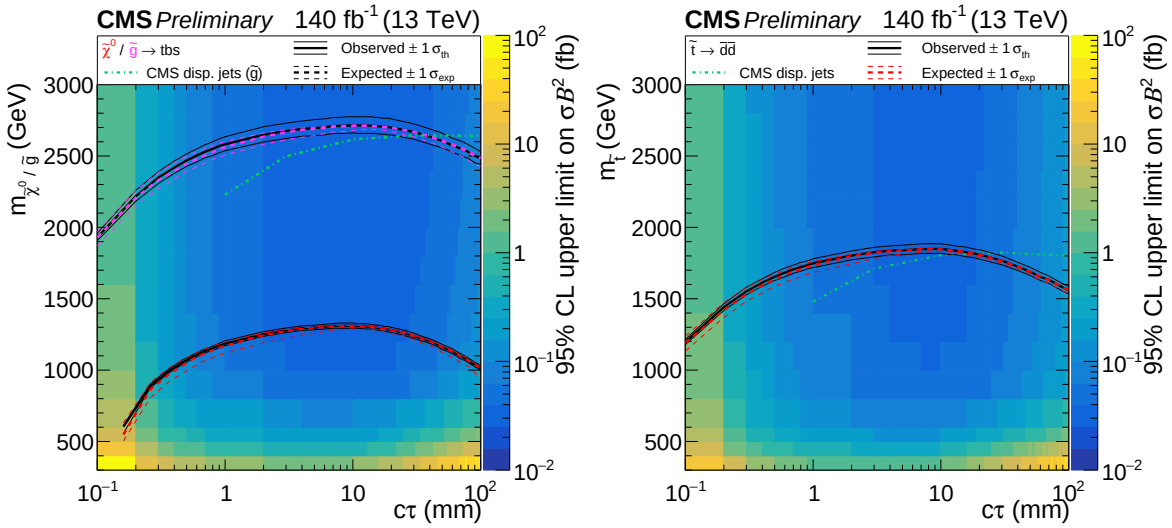


Figure 7: Observed 95% CL upper limits on cross section times branching fraction squared for the multijet (left) and dijet (right) signals as a function of mass and $c\tau$. The overlaid mass-lifetime exclusion curves assume pair-production cross sections for the neutralino (red) and gluino (pink) in multijet signals and top squark cross sections for the dijet signals with 100% branching fraction to each model's respective decay mode specified. The solid black (dashed colored) lines represent the observed (median expected) limits at 95% CL. The thin black lines represent the variation of the observed limit within theoretical uncertainties of the signal cross section. The thin dashed colored lines represent the region containing 68% of the expected limit distribution under the background-only hypothesis. The observed limits from the CMS displaced jets search [29] are also shown in green for comparison.

For the long-lived gluino, neutralino, and top squark in the RPV models described, pair pro-

duction cross sections larger than 0.08 fb are excluded for masses between 800 and 3000 GeV and mean proper decay lengths between 1 and 25 mm. For mean proper decay lengths between 0.6 and 90 mm, the data exclude gluino masses up to 2500 GeV; for mean proper decay lengths between 0.6 and 70 mm, the data exclude neutralino masses up to 1100 GeV; and for mean proper decay lengths between 0.4 and 80 mm, the data exclude top squark masses up to 1600 GeV. These are the most stringent bounds on these models for mean proper decay lengths between 100 $\mu$m and 15 mm for all masses considered. In contrast, prompt searches have only excluded pair-produced prompt gluinos decaying into trijet final states for masses up to 1500 GeV and prompt top squarks decaying into dijet final states for masses up to 520 GeV [53, 54]. The potential long lifetime of the particle provides a handle to reduce the background and allows this search to have better sensitivity to larger masses.

Figure 8 shows one-dimensional slices of the upper limit as a function of mass for several values of $c\tau$. Similarly, Fig. 9 shows the the upper limit as a function of $c\tau$ for a selection of masses.

At a specific signal point, a gluino with a mass of 800 GeV and mean proper decay length $c\tau$ of 1 mm, the computed 95% CL upper limit on $\sigma\mathcal{B}^2$ in the 2017 and 2018 dataset alone is 0.11 fb, compared with the limit from the 2015 and 2016 dataset of 0.3 fb. The improvements arise primarily from the increase in statistical precision due to the increased integrated luminosity of 101 $\text{fb}^{-1}$ compared with 38.5 $\text{fb}^{-1}$. By combining these two datasets, the 95% CL upper limit for the same signal point moves further down to 0.08 fb.

# 11 Summary

We present a search for pair-produced long-lived particles decaying into multijet and dijet final states using proton-proton collision events collected with the CMS detector at a center-of-mass energy of 13 TeV during the full Run 2 data collection period, corresponding to an integrated luminosity of 140 $\text{fb}^{-1}$. No events were observed in the signal region in the 2017 and 2018 datasets, and no excess yield beyond the standard model prediction is observed in the full Run 2 dataset. At 95% CL, upper limits are set for an RPV SUSY model in which a long-lived neutralino or gluino decays into a multijet final state with top, bottom, and strange antiquarks. Signal pair-production cross sections larger than 0.08 fb are excluded for long-lived neutralino, gluino, and top squark masses between 800 and 3000 GeV and mean proper decay lengths between 1 mm and 25 mm. For the range of mean proper decay lengths between 0.6 and 90 mm, the data exclude gluino masses up to 2500 GeV. For a neutralino LSP, the data exclude neutralino masses up to 1100 GeV for mean proper decay lengths between 0.6 and 70 mm. Additionally, limits are placed for an RPV SUSY model in which a long-lived top squark decays into a dijet final state with two down antiquarks. The data exclude top squark masses up to 1600 GeV for mean proper decay lengths between 0.4 and 80 mm. These are the most stringent bounds on these models for $c\tau$ between 100 $\mu$m and 15 mm for all masses considered, complementing the results of the CMS displaced jet search [29]. While the search directly constrains these two RPV SUSY models, the techniques and methodology are generic and the results are applicable to other models of pair-produced long-lived particles that decay into jets. A method is provided in Appendix A to facilitate the reinterpretation of these results for alternative models.

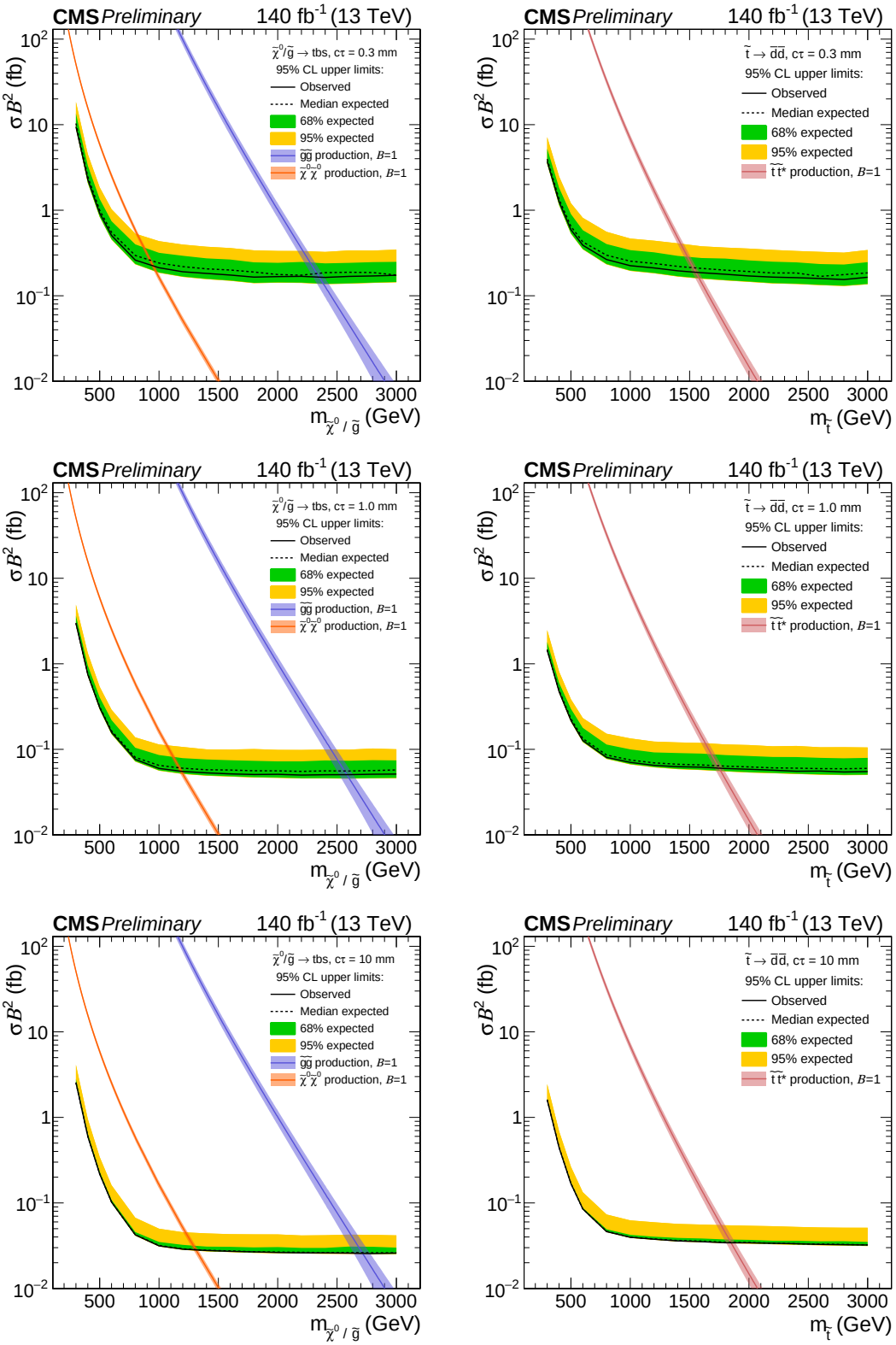


Figure 8: Observed and expected 95% CL upper limits on cross section times branching fraction squared as a function of mass for multijet signals (left) and dijet signals (right), for a fixed $c\tau$ of 0.3 mm (top), 1 mm (middle), and 10 mm (bottom) in the full Run 2 data set. The neutralino and gluino pair production cross sections are overlaid for the multijet signals, and the top squark pair production cross section is overlaid for the dijet signals.

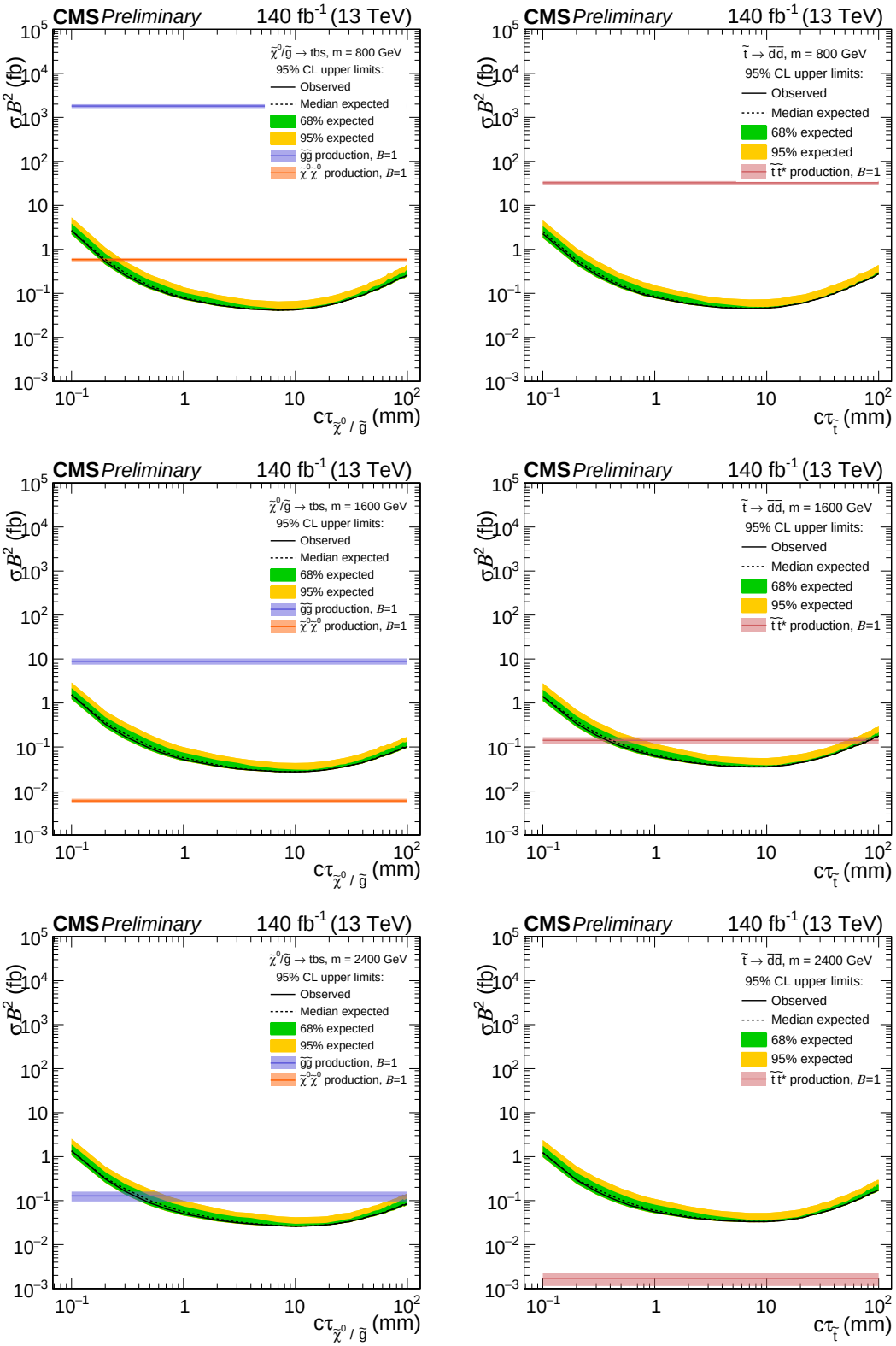


Figure 9: Observed and expected 95% CL upper limits on cross section times branching fraction squared as a function of $c\tau$ for multijet signals (left) and dijet signals (right), for a fixed mass of 800 GeV (top), 1600 GeV (middle), and 2400 GeV (bottom) in the full Run 2 data set. The neutralino and gluino pair production cross sections are overlaid for the multijet signals, and the top squark pair production cross section is overlaid for the dijet signals.

## References


[1] R. Barbier et al., "*R*-parity violating supersymmetry", *Phys. Rept.* **420** (2005) 1, doi:10.1016/j.physrep.2005.08.006, arXiv:hep-ph/0406039.

[2] C. Csáki, Y. Grossman, and B. Heidenreich, "Minimal flavor violation supersymmetry: a natural theory for *R*-parity violation", *Phys. Rev. D* **85** (2012) 095009, doi:10.1103/PhysRevD.85.095009, arXiv:1111.1239.

[3] C. Csáki et al., "Phenomenology of a long-lived LSP with *R*-parity violation", *JHEP* **08** (2015) 016, doi:10.1007/JHEP08(2015)016, arXiv:1505.00784.

[4] L. J. Hall and M. Suzuki, "Explicit *R*-parity breaking in supersymmetric models", *Nucl. Phys. B* **231** (1984) 419, doi:10.1016/0550-3213(84)90513-3.

[5] N. Arkani-Hamed and S. Dimopoulos, "Supersymmetric unification without low energy supersymmetry and signatures for fine-tuning at the LHC", *JHEP* **06** (2005) 073, doi:10.1088/1126-6708/2005/06/073, arXiv:hep-th/0405159.

[6] N. Arkani-Hamed, S. Dimopoulos, G. F. Giudice, and A. Romanino, "Aspects of split supersymmetry", *Nucl. Phys. B* **709** (2005) 3, doi:10.1016/j.nuclphysb.2004.12.026, arXiv:hep-ph/0409232.

[7] N. Arkani-Hamed et al., "Simply unnatural supersymmetry", 2012.

[8] A. Arvanitaki, N. Craig, S. Dimopoulos, and G. Villadoro, "Mini-split", *JHEP* **02** (2013) 126, doi:10.1007/JHEP02(2013)126, arXiv:1210.0555.

[9] P. Gambino, G. F. Giudice, and P. Slavich, "Gluino decays in split supersymmetry", *Nucl. Phys. B* **726** (2005) 35, doi:10.1016/j.nuclphysb.2005.08.011, arXiv:hep-ph/0506214.

[10] G. F. Giudice and A. Romanino, "Split supersymmetry", *Nucl. Phys. B* **699** (2004) 65, doi:10.1016/j.nuclphysb.2004.08.001, arXiv:hep-ph/0406088. [Erratum: doi:10.1016/j.nuclphysb.2004.11.048].

[11] J. L. Hewett, B. Lillie, M. Masip, and T. G. Rizzo, "Signatures of long-lived gluinos in split supersymmetry", *JHEP* **09** (2004) 070, doi:10.1088/1126-6708/2004/09/070, arXiv:hep-ph/0408248.

[12] T. Han, Z. Si, K. M. Zurek, and M. J. Strassler, "Phenomenology of hidden valleys at hadron colliders", *JHEP* **07** (2008) 008, doi:10.1088/1126-6708/2008/07/008, arXiv:0712.2041.

[13] M. J. Strassler and K. M. Zurek, "Echoes of a hidden valley at hadron colliders", *Phys. Lett. B* **651** (2007) 374, doi:10.1016/j.physletb.2007.06.055, arXiv:hep-ph/0604261.

[14] M. J. Strassler and K. M. Zurek, "Discovering the Higgs through highly-displaced vertices", *Phys. Lett. B* **661** (2008) 263, doi:10.1016/j.physletb.2008.02.008, arXiv:hep-ph/0605193.

[15] J. Fan, M. Reece, and J. T. Ruderman, "Stealth supersymmetry", *JHEP* **11** (2011) 012, doi:10.1007/JHEP11(2011)012, arXiv:1105.5135.

[16] J. Fan, M. Reece, and J. T. Ruderman, "A stealth supersymmetry sampler", *JHEP* **07** (2012) 196, doi:10.1007/JHEP07(2012)196, arXiv:1201.4875.

[17] L. Calibbi, L. Lopez-Honorez, S. Lowette, and A. Mariotti, "Singlet-Doublet dark matter freeze-in: LHC displaced signatures versus cosmology", *JHEP* **09** (2018) 037, doi:10.1007/JHEP09(2018)037, arXiv:1805.04423.

[18] R. T. Co, F. D'Eramo, L. J. Hall, and D. Pappadopulo, "Freeze-In dark matter with displaced signatures at colliders", *JCAP* **1512** (2015) 024, doi:10.1088/1475-7516/2015/12/024, arXiv:1506.07532.

[19] Y. Cui, L. Randall, and B. Shuve, "A WIMPy baryogenesis miracle", *JHEP* **04** (2012) 075, doi:10.1007/JHEP04(2012)075, arXiv:1112.2704.

[20] Y. Cui and R. Sundrum, "Baryogenesis for weakly interacting massive particles", *Phys. Rev. D* **87** (2013) 116013, doi:10.1103/PhysRevD.87.116013, arXiv:1212.2973.

[21] Y. Cui and B. Shuve, "Probing baryogenesis with displaced vertices at the LHC", *JHEP* **02** (2015) 049, doi:10.1007/JHEP02(2015)049, arXiv:1409.6729.

[22] L. J. Hall, K. Jedamzik, J. March-Russell, and S. M. West, "Freeze-in production of FIMP dark matter", *JHEP* **03** (2010) 080, doi:10.1007/JHEP03(2010)080, arXiv:0911.1120.

[23] D. E. Kaplan, M. A. Luty, and K. M. Zurek, "Asymmetric dark matter", *Phys. Rev. D* **79** (2009) 115016, doi:10.1103/PhysRevD.79.115016, arXiv:0901.4117.

[24] I.-W. Kim and K. M. Zurek, "Flavor and collider signatures of asymmetric dark matter", *Phys. Rev. D* **89** (2014) 035008, doi:10.1103/PhysRevD.89.035008, arXiv:1310.2617.

[25] CMS Collaboration, "Search for long-lived particles with displaced vertices in multijet events in proton-proton collisions at $\sqrt{s} = 13$ TeV", *Phys. Rev. D* **98** (2018) 092011, doi:10.1103/PhysRevD.98.092011, arXiv:1808.03078.

[26] CMS Collaboration, "CMS Technical Design Report for the Pixel Detector Upgrade", doi:10.2172/1151650.

[27] ATLAS Collaboration, "Search for long-lived, massive particles in events with displaced vertices and missing transverse momentum in $\sqrt{s}$ = 13 TeV $pp$ collisions with the ATLAS detector", *Phys. Rev. D* **97** (2018) 052012, doi:10.1103/PhysRevD.97.052012, arXiv:1710.04901.

[28] ATLAS Collaboration, "Search for long-lived, massive particles in events with a displaced vertex and a muon with large impact parameter in $pp$ collisions at $\sqrt{s} = 13$ TeV with the ATLAS detector", arXiv:2003.11956.

[29] CMS Collaboration, "Search for long-lived particles decaying into displaced jets", Technical Report CMS-PAS-EXO-19-021, CERN, Geneva, 2020.

[30] CMS Collaboration, "The CMS experiment at the CERN LHC", *JINST* **3** (2008) S08004, doi:10.1088/1748-0221/3/08/S08004.

[31] CMS Collaboration, "Track impact parameter resolution in the 2017 dataset with the CMS Phase-1 Pixel detector", CMS Detector Performance Summary CMS-DP-2020-032, CERN, 2020.

[32] CMS Collaboration, "The CMS trigger system", *JINST* **12** (2017) P01020, doi:10.1088/1748-0221/12/01/P01020, arXiv:1609.02366.

[33] CMS Collaboration, "Particle-flow reconstruction and global event description with the CMS detector", *JINST* **12** (2017) P10003, doi:10.1088/1748-0221/12/10/P10003, arXiv:1706.04965.

[34] M. Cacciari, G. P. Salam, and G. Soyez, "The anti-$k_t$ jet clustering algorithm", *JHEP* **04** (2008) 063, doi:10.1088/1126-6708/2008/04/063, arXiv:0802.1189.

[35] M. Cacciari, G. P. Salam, and G. Soyez, "FastJet user manual", *Eur. Phys. J. C* **72** (2012) 1896, doi:10.1140/epjc/s10052-012-1896-2, arXiv:1111.6097.

[36] CMS Collaboration, "Jet energy scale and resolution in the CMS experiment in pp collisions at 8 TeV", *JINST* **12** (2017) P02014, doi:10.1088/1748-0221/12/02/P02014, arXiv:1607.03663.

[37] T. Sjöstrand et al., "An Introduction to PYTHIA 8.2", *Comput. Phys. Commun.* **191** (2015) 159, doi:10.1016/j.cpc.2015.01.024, arXiv:1410.3012.

[38] NNPDF Collaboration, "Parton distributions from high-precision collider data", *Eur. Phys. J.* **C77** (2017) 663, doi:10.1140/epjc/s10052-017-5199-5, arXiv:1706.00428.

[39] CMS Collaboration, "Extraction and validation of a new set of CMS PYTHIA8 tunes from underlying-event measurements", *Eur. Phys. J. C* **80** (2020) 4, doi:10.1140/epjc/s10052-019-7499-4, arXiv:1903.12179.

[40] J. Alwall et al., "The automated computation of tree-level and next-to-leading order differential cross sections, and their matching to parton shower simulations", *JHEP* **07** (2014) 079, doi:10.1007/JHEP07(2014)079, arXiv:1405.0301.

[41] NNPDF Collaboration, "Parton distributions for the LHC Run II", *JHEP* **04** (2015) 040, doi:10.1007/JHEP04(2015)040, arXiv:1410.8849.

[42] J. Alwall et al., "Comparative study of various algorithms for the merging of parton showers and matrix elements in hadronic collisions", *Eur. Phys. J. C* **53** (2008) 473, doi:10.1140/epjc/s10052-007-0490-5, arXiv:0706.2569.

[43] GEANT4 Collaboration, "GEANT4—a simulation toolkit", *Nucl. Instrum. Meth. A* **506** (2003) 250, doi:10.1016/S0168-9002(03)01368-8.

[44] CMS Collaboration, "Identification of heavy-flavour jets with the CMS detector in pp collisions at 13 TeV", *JINST* **13** (2018) P05011, doi:10.1088/1748-0221/13/05/P05011, arXiv:1712.07158.

[45] J. Butterworth et al., "PDF4LHC recommendations for LHC Run II", *J. Phys. G* **43** (2016) 023001, doi:10.1088/0954-3899/43/2/023001, arXiv:1510.03865.

[46] CMS Collaboration, "CMS luminosity measurement for the 2017 data-taking period at $\sqrt{s} = 13\,\text{TeV}$", CMS Physics Analysis Summary CMS-PAS-LUM-17-001, CERN, 2018.

[47] CMS Collaboration, "CMS luminosity measurement for the 2018 data-taking period at $\sqrt{s} = 13\,\text{TeV}$", CMS Physics Analysis Summary CMS-PAS-LUM-18-002, CERN, 2019.

[48] C. Borschensky et al., "Squark and gluino production cross sections in pp collisions at $\sqrt{s} = 13$, 14, 33 and 100 TeV", *Eur. Phys. J. C* **74** (2014) 3174, doi:10.1140/epjc/s10052-014-3174-y, arXiv:1407.5066.

[49] W. Beenakker et al., "NNLL resummation for stop pair-production at the LHC", *JHEP* **05** (2016) 153, doi:10.1007/JHEP05(2016)153, arXiv:1601.02954.

[50] M. Beneke, J. Piclum, C. Schwinn, and C. Wever, "NNLL soft and Coulomb resummation for squark and gluino production at the LHC", *JHEP* **10** (2016) 054, doi:10.1007/JHEP10(2016)054, arXiv:1607.07574.

[51] B. Fuks, M. Klasen, D. R. Lamprea, and M. Rothering, "Gaugino production in proton-proton collisions at a center-of-mass energy of 8 TeV", *JHEP* **10** (2012) 081, doi:10.1007/JHEP10(2012)081, arXiv:1207.2159.

[52] B. Fuks, M. Klasen, D. R. Lamprea, and M. Rothering, "Precision predictions for electroweak superpartner production at hadron colliders with RESUMMINO", *Eur. Phys. J. C* **73** (2013) 2480, doi:10.1140/epjc/s10052-013-2480-0, arXiv:1304.0790.

[53] CMS Collaboration, "Search for pair-produced resonances decaying to quark pairs in proton-proton collisions at $\sqrt{s} = 13$ TeV", *Phys. Rev. D* **98** (2018), no. 11, 112014, doi:10.1103/PhysRevD.98.112014, arXiv:1808.03124.

[54] CMS Collaboration, "Search for pair-produced three-jet resonances in proton-proton collisions at $\sqrt{s}$ =13 TeV", *Phys. Rev. D* **99** (2019), no. 1, 012010, doi:10.1103/PhysRevD.99.012010, arXiv:1810.10092.

# A Extending results to different signal models

While the search presented specifically addresses two models of RPV SUSY, the results may be applied to other models in which the pair-produced long-lived particle decays into two or more jets in the final state. Conversion of the upper limit on signal events to an upper limit on the corresponding signal cross section depends on the reconstruction efficiency for that model. In this section, we present a set of generator-level selection requirements that, when applied, approximate the reconstruction-level efficiency of this analysis and allow for a reinterpretation of the results.

Event selection is based on generated jet properties and the properties of the constituent long-lived particles and their daughter decay products. We assume that the generated jets are clustered from all final state particles, excluding neutrinos, using the anti-$k_{\mathrm{T}}$ algorithm with a distance parameter of 0.4. A jet is rejected if the fraction of energy shared by electrons is greater than 0.9, or similarly if the muon energy fraction is greater than 0.8. We apply additional kinematic requirements at the parton level where the daughter particles considered are the u, d, s, c, and b quarks in addition to the electron, muon, and tau leptons from the long-lived particle decay. These daughter particles must have a transverse impact parameter with respect to the origin of at least 0.1 mm. To be selected, generated jets and the daughter particles are required to satisfy $p_{\mathrm{T}} > 20\,\mathrm{GeV}$ and $|\eta| < 2.5$.

The following generator-level selection requirements approximate the reconstruction-level criteria:

- each event must contain at least four generated jets
- $H_{\mathrm{T}} > 1200\,\mathrm{GeV}$, where $H_{\mathrm{T}}$ is the scalar sum of the $p_{\mathrm{T}}$ of generated jets with $p_{\mathrm{T}} > 40\,\mathrm{GeV}$
- the distance of decay point from the origin in the $x$-$y$ plane of each generated long-lived particle must be within 0.1 and 20 mm
- the $\Sigma p_{\mathrm{T}}$ of the daughter particles of each long-lived particle must exceed 350 GeV to ensure sufficiently small uncertainty in $d_{\mathrm{BV}}$ and sufficiently large number of tracks per vertex. However, if the daughter particle is a b quark its $\Sigma p_{\mathrm{T}}$ is scaled down by a factor of 0.65. This corrects for the reduced efficiency at reconstruction-level due to the lifetime of the b quark that can inhibit the association of the decay products to the reconstructed vertex.
- the transverse distance between the decay points of each long-lived particle must be greater than 0.4 mm

Following this prescription, the generator-level efficiency approximates the reconstruction-level efficiency with 20% accuracy for a wide variety of models that have signal efficiency of 10% or more. This was tested for models with both dijet and multijet final states for masses between 400 GeV and 3000 GeV and lifetimes between 100 $\mu$m and 30 mm. This prescription has not been validated for models that have efficiencies lower than 10%.